nature nanotechnology

Supplementary information https://doi.org/10.1038/s41565-024-01793-0

Mechanochemistry-mediated colloidal liquid metals for electronic device cooling at kilowatt levels

In the format provided by the authors and unedited

Table of Contents:

Section 1

Supplementary Table S1 | Status of current cooling techniques.

Comparisons of thermal management ability of cooling techniques in previous studies.

Cooling technique	Note	Size (cm^2)	Heat flux (W/cm^2)	Experiment/ simulation	Heat source-heat sink interface	Reference
Air-free convection	Ceramic heater	1	5	Experiment	Vertical graphene	1
	LED	2.23	4.48	Experiment	Thermal pad	2
	Smart phone	1.58	2.98	Experiment	Thermal pad	3
	Laser heated Al block	0.35	0.96	Experiment	Thermal pad	4
	CPU	14.06	6.75	Experiment	Thermal grease	/
	Battery	/	0.17	Experiment	/	5
Air-forced convection	Chip	1	9	Experiment	Thermal gel	6
	Ceramic heater	4	70	Experiment	Vertical graphene	7
	LED	3	6.67	Experiment	Vertical graphene	8
	Chips in data center	5.96	30	Experiment	Direct contact	9
	Chips in data center	5.96	50	Experiment	Direct contact	9
	Chips in data center	5.96	51	Experiment	Direct contact	9
Single-phase microchannel cooling	Water fluid	4	50	Experiment	Vertical graphene/LM	10
	Water fluid, diamond on SiC microchannel	0.06	3000	Experiment	Sn–3.5Ag solder	11
	Water fluid, silicon microchannel	1	790	Experiment	Direct contact	12
	Liquid metal fluid, copper mini-channel	4.48	242	Experiment	/	13
	Water fluid, copper microchannel	4.70	100	Experiment	/	14
	Liquid metal fluid, copper mini-channel	5	300	Experiment	/	15
	Water fluid, silicon manifold	0.081	1700	Experiment	/	16
	Water fluid, silicon microchannel	/	1000	Simulation	/	17
	Water fluid, silicon-diamond microchannel	0.04	1600	Simulation	/	18
	Liquid metal fluid, copper microchannel	0.5	200	Experiment	/	19
Two-phase microchannel cooling	Hydrofluoroether fluid, silicon microchannel	0.06	700	Experiment	Direct contact, metal sputterers	20
	/	0.01	365	Experiment	/	21
	Ammonia fluid, diamond microchannel	0.10	1000.4	Experiment	/	22
	Pentane and R245fa fluid, silicon microchannel	0.017	665	Experiment	Direct contact, deposited platinum	23

	Water/sodium lauryl sulfate fluid, silicon microchannel	20.16	29.4	Experiment	/	24
	Water fluid, silicon microchannel	0.2	506	Experiment	/	25
	Water fluid, silicon microchannel	0.25	380	Experiment	Direct contact, deposited platinum	26
	Water fluid, copper microchannel	1	82	Experiment	/	27
	Water fluid, silicon microchannel	0.032	859	Experiment	Direct contact, deposited metal	28
Spray cooling	Ammonia fluid	3	350	Experiment	Thermal grease	29
	Water fluid	1.69	643.4	Experiment	/	30
	Water fluid	1	1200	Experiment	/	31
	Water fluid	1.3	830	Experiment	/	32
	Ammonia fluid	2	910	Experiment	/	33
	Water fluid	2	600	Experiment	/	34
	Water fluid	1.44	705	Experiment	/	35
Jet impingement	Water fluid	0.058	284	Experiment	/	36
	Fluorinert FC-72 fluid	1.61	400	Experiment	/	37
	Water fluid	2.92	300	Experiment	/	38
	Ammonia fluid	0.06	1367	Experiment	/	39
	Water fluid	5.06	255	Experiment	/	40
	Water fluid	2.85	674	Experiment	/	41
	Water fluid	1	1110	Experiment	/	42
Single-phase microchannel cooling	Water fluid, Al/diamond microchannel	16	90	Experiment	LM/AlN composite	This work
		16	100	Experiment	Noctua NT-H2, thermal grease	
		16	100	Experiment	SYY 157, thermal grease	
		16	120	Experiment	Thermal Grizzly Kryonaut, thermal grease	
		16	120	Experiment	DOWSIL TC-5026, thermal grease	
		16	200	Experiment	Colloidal LM-1 μm	
		16	200	Experiment	Colloidal LM-5 μm	
		16	200	Experiment	Colloidal LM-30 μm	
		16	200	Experiment	Colloidal LM-80 μm	
		16	400	Simulation	Colloidal LM-30 μm	

Section 2

Supplementary Table 2 | Power density of the current semiconductor power electronic devices. *Power density of the current semiconductor power electronic devices, including CPU, FPGA, GPU, SiC transistor, and GaN transistor.*

Type	Model	Power (W)	Area (cm^2)	Heat flux (W/cm^2)	Reference
CPU	i5-1260U	9	2.17	4.15	/
	i5-1260P	28	2.17	12.90	/
	Platinum 8470/2023	350	19.08	18.34	/
	EPYC 7601/2017	180	4.20	42.86	/
	Threadripper 1950X/2017	180	4.26	42.25	/
	Threadripper 2990WX/2018	250	8.52	29.34	/
	EPYC 7H12/2019	280	6.66	42.04	/
	Threadripper 3995WX/2020	280	5.92	47.29	/
	EPYC 7763/2021	280	6.48	43.21	/
	EPYC 9654/2022	360	8.64	41.67	/
	EPYC 9684X/2023	400	8.64	46.30	/
FPGA	Xlinx Spartan 6	/	0.64	63	[43]
	Intel Stratix 10	/	25	12	[43]
GPU	Nvidia GP102/2017	250	4.71	53.08	/
	Nvidia TU102/2018	250	7.54	33.16	/
	Nvidia GA102/2020	350	6.28	56.00	/
	Nvidia AD102/2022	450	6.09	73.89	/
	Nvidia GA100/2020	400	8.26	48.42	/
	Nvidia GH100/2022	700	8.14	85.99	/
SiC transistor	STM SCTH35N65G2V-7	/	1.19	175	[43]
	SLSIC1MO120E0080	/	3.12	181	[43]
	STM SCTW100N120G2AG	/	2.46	73	[43]
	NTBG040N120SC1	/	9.10	195	[43]
	NVH4L020N120SC1	/	2.11	121	[43]
GaN transistor	GS0650041L	7.2	0.30	24	[43]
	GS0650111L	18	0.30	60	[43]
	GS61004B	22.8	0.20	114	[43]
	GS61008P	56.1	0.34	165	[43]
	GS0651501D	223.3	0.70	319	[43]
	GS0650801D	115.4	0.37	312	[43]

Section 3

Theoretical calculation of the thermal conductivity and effective thermal interface resistance of polymer composites

The differential effective medium model of Bruggeman is used to predict the thermal conductivity of polymer composites.[44,45] It derives the expression for the effective thermal conductivity of a two-phase material with nonzero interfacial thermal resistance. This formula describes the dependence of the thermal conductivity on the filler particle radius, and the boundary conductivity that is the reciprocal of interfacial thermal resistance. The equation is provided as follows:

$$1 - V_d = \frac{k_c - k_d^{eff}}{k_m - k_d^{eff}} \left(\frac{k_m}{k_c}\right)^{1/n}$$

$$k_d^{eff} = \frac{k_d^{in}}{1 + k_d^{in}/(a \times h_c)}$$

where k_c is effective thermal conductivity of the composite; k_m is thermal conductivity of the polymer matrix; k_d^{in} is thermal conductivity of the particle; a is particle radius; h_c is the reciprocal of interfacial thermal resistance; V_d is particle volume fraction; n is the shape factor. Noted that n=3 is for the spherical particles.

Herein, polydimethylsiloxane (PDMS) composites filled with AlN particles were taken as an example of the TIM. To predict the thermal conductivity as a function of the particle radius (0.5, 2.5, 15 and 40 μm), the thermal conductivity of PDMS is 0.15 W m^{-1} K^{-1}, the thermal conductivity of AlN is 220 W m^{-1} K^{-1} because of taking the oxygen impurities into consideration,[46,47] and good interfacial thermal resistance between filler and matrix is assumed (1×10^{-8} m^2 K/W). The calculated results are plotted in Extended Data Fig. 1a.

The effective thermal interface resistance of a TIM can be divided into three parts, represented by the following formula:

$$R_{eff} = \frac{BLT}{k} + R_{c1} + R_{c2}$$

where R_{eff} is the effective thermal interface resistance in a sandwiched structure; *BLT* is the bond line thickness of a TIM; k is the thermal conductivity; R_{c1} and R_{c2} are the contact thermal resistance with the heat sink and heat source.

To predict the relationship between *BLT* and R_{eff} when the PDMS/AlN composites serve as the TIM, k is firstly predicted according to the differential effective medium model of Bruggeman. Herein, to ensure the excellent thixotropy and promising good conformability with the heat source and the heat sink, the PDMS/AlN composites should keep their grease state. Therefore, the approximately highest filling of 73 vol% is selected for AlN particles. Secondly, the R_c between the PDMS/AlN composites and the double substrates is predicted according to theoretical polymer-dielectric interfacial thermal resistance and experimental results of the commercial greases. Previous studies indicate that ideal polymer-dielectric interfacial thermal resistance lies in the range from 10^{-7} to 10^{-6} m^2 K/W.[48,49] And we directly measured the R_c of some commercial thermal greases, whose value is 1.31±0.23 mm^2 K/W for Shin-Etsu 7921, 1.42±0.26 mm^2 K/W for Aigo-PRO, 2.47±0.19 mm^2 K/W for Linkstone, and 0.55±0.113 mm^2 K/W for DOWSIL 5026. Therefore, in this prediction, the R_c is set as the lowest value of 0.55 mm^2 K/W. Based on the above assumptions and results, the relationship between *BLT* and R_{eff} are plotted in Extended Data Fig. 1b.

According to the above theoretical calculations, only when the *BLT* is on the order of micrometers, the R_{eff} of PDMS composites filled with highly thermally conductive inorganics falls within the narrow range of 0.1-1 mm^2 K/W. This implies a high level of thixotropy in these polymer composites, exerting compressive forces near the *BLT* limit, adjacent to the particle diameter. However, achieving such a property at a high particle content (>70 vol%) poses a significant challenge using current material engineering strategies. Moreover, the micron-sized *BLT* will be constrained in practical thermal management applications, particularly for large-area powered electronics, where significant thermal expansion mismatch could occur between polymer TIMs and solid substrates.

Section 4

Theoretical calculation of the thermal conductivity and effective thermal interface resistance of LMs

To predict the thermal conductivity of LM/AlN colloids as a function of the interfacial thermal resistance, herein, the thermal conductivity of LM (Galinstan) is 26.08 W m^{-1} K^{-1} that is measured with ASTM D5470 standard, the thermal conductivity of AlN is 220 W m^{-1} K^{-1}, and the interface thermal resistance between AlN and matrix is valued as 1×10^{-6} m^2 K/W, 1×10^{-7} m^2 K/W, 1×10^{-8} m^2 K/W, 1×10^{-9} m^2 K/W, and 1×10^{-10} m^2 K/W, respectively. The results in Extended Data Fig. 1c plot the thermal conductivity of the LM/AlN colloids as a function of the AlN content, taking the particle radius of 15 µm as an example.

To predict the functional relationship between *BLT* and R_{eff} when the LM/AlN colloids serve as the TIM, firstly, the *k* is calculated according to the differential effective medium model of Bruggeman. Similar to the above paragraph, we assume that the interfacial thermal resistance between AlN and LM matrix is 1×10^{-6}, 1×10^{-7}, 1×10^{-8}, 1×10^{-9}, and 1×10^{-10} m^2 K/W. Therefore, the *k* could be obtained as a function of the filler content and the particle size. Herein, the thermal conductivity of LM is 26.08 W m^{-1} K^{-1}, the thermal conductivity of AlN is 220 W m^{-1} K^{-1}, the AlN content is about 40 vol% for promising the thixotropy, and the particle diameter is valued as 1 µm, 5 µm, 30 µm, and 80 µm, respectively. It was reported that metal-metal interface always exhibits much larger interfacial thermal conductance ranging from 0.1-10 GW/m^2 K.[50] If colloidal LMs can be perfectly conformable to the rough surface of the substrates, the R_c between the colloidal LMs and the double substrates is predicted to be lower than 0.1 mm^2 K/W. Based on the above assumptions and results, the predicted relationship between *BLT* and R_{eff} is plotted in Extended Data Fig. 1d-g.

According to the above calculations based on the differential effective medium model of Bruggeman, a significant increase in the *k* of AlN-modified LMs is observed only when the interfacial thermal resistance between AlN and LM reaches values on the order of 10^{-9} m^2 K/W (Extended Data Fig. 1c). This places stringent demands on manipulating the metal-dielectric interface within the two-phase mixtures.

As depicted in Extended Data Fig. 1d-g, AlN particles with diameters ranging from 1 to 30 µm are likely to enable LMs to achieve an effective R_{eff} on the order of 0.1 mm^2 K/W. This achievement necessitates not only particular regulation of the LM-AlN interface but also exceptional thixotropy and adaptability to rough surfaces. The latter considerations are crucial for modified LMs to attain a low *BLT* and R_c in a sandwiched structure, respectively.

Section 5

Predicting material combinations for future fabrication of colloidal LMs

The colloidal LMs in this study were synthesized via a mechanochemical approach, in which substantial force propelled the LM to infiltrate the crystal lattice of the ceramic particle, establishing efficient LM-solid interactions by coordinating the unoccupied orbit of metal atoms in the LM with the lone pair electrons of nitrogen atoms in the AlN. It is possible that this mechanochemical effect is also applicable to versatile material combinations between general liquid metals and universal ceramics containing abundant characteristic atoms with lone pair electrons. For example, some room-temperature liquid metals like Ga, $GaIn_{21.4}$, $GaSn_{13.4}$, $GaAl_{0.9}$ and Galinstan can be the choice of the LM host. For the solid particles, general ceramics containing abundant nitrogen, oxygen, fluorine, sulfur, or chlorine atoms could be the candidates, for example, Al_2O_3, SiO_2, WO_3, ZnO, BN, Si_3N_4, or MoS_2. These particles allow the formation of robust coordination with the LMs at the liquid-solid interface. However, the interplanar spacing of crystal lattice is necessarily large enough for the efficient infiltration of metal atoms. Based on the above material combinations, multifunctional colloidal LMs for various applications could be expected in future studies.

Section 6

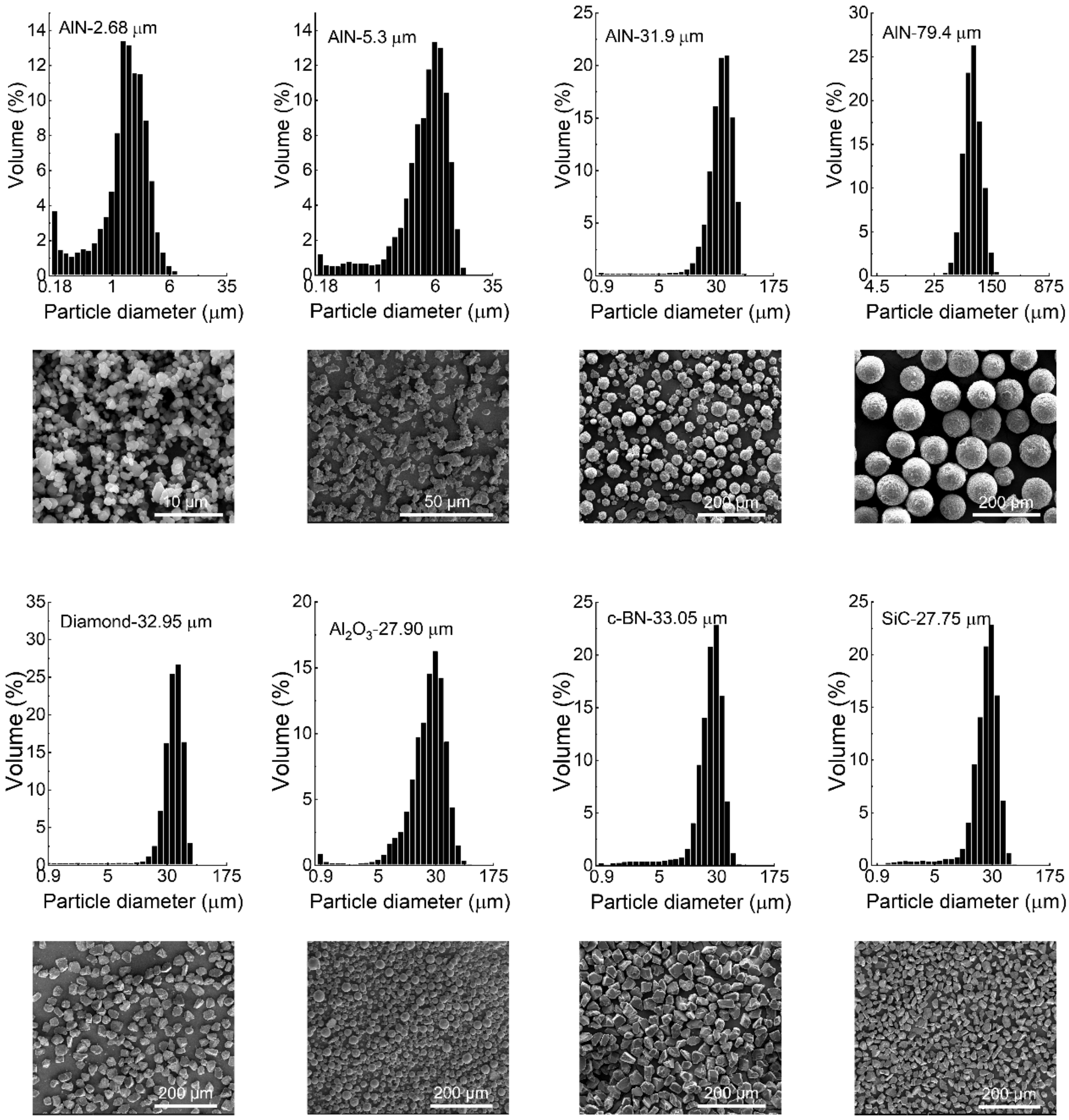

Supplementary Fig. 1 | Statistics of particle diameter. *Four types of AlN, including 1 µm, 5 µm, 30 µm and 80 µm, and the other four different thermally conductive particles for comparisons are characterized to determine the average diameter.*

Section 7

Supplementary Table 3 | Comparative analysis of thermal interface performance between colloidal LMs and TIMs from previous studies. *Most TIMs are dry-contact type except for some special nanowire arrays. Note that Shin-Etsu X-23, Thermalright TF-X, Thermalright TF-8 and DOWSIL TC-5026 are four different commercial thermal greases. Laird 720 and Bergquist 5000S35 are two different commercial thermal pads. Their thermal properties are also tested in the lab for comparative studies.*

Type	Material	*BLT* (μm)	R_c (mm^2 K/W)	$R_{eff, bonded contact}$ (mm^2 K/W)	$R_{eff, dry contact}$ (mm^2 K/W)	Ref.
Nanowire array	Si-CNTs/P3HT-Ag	10	/	4.90 ± 0.30	/	51
	Si-CNTs/PyprPA-Cu-Ag	15	/	4.60 ± 0.50	40 ± 20	52
	Ti-CNTs-Au	30	/	10 ± 0.50	/	53
	Ti-CNT-Au	130	/	10 ± 0.50	/	53
	Si-CNTs/APS-glass	/	0.60	3.50±0.50	/	54
	Si-CuNW/Sn-Si	14	/	0.51 ± 0.09	/	55
	Cu-CuNW/ Graphene/Sn-Cu	≤40	/	0.26± 0.02	/	56
	Si-CNTs/In-Au	10	/	1	/	57
	CNTs	300	/	/	77	58
	CNTs	25	/	/	7 ± 0.50	59
	CNTs	50	/	/	8 ± 1	60
	CNTs	15	/	/	20 ± 6	51
Vertical graphene	Graphene array	19	11.42	/	11.77	1
	Graphene nanowalls	100	23.70	/	28.57	61
	Graphene monolith	810	20.20	/	26.90	7
	Graphene monolith	630	5.80	/	11.80	7
	Graphene/SiC	250	47	/	61	62
	Graphene/PU	750	66	/	70.50	63
	Graphene/PU/Au	1656	41	/	47	63
	Graphene monolith	2300	10.20	/	30.50	64
Solder	Solder A	257	1.80	/	5.70	65
	Solder B	295	2.90	/	8.10	65
	Solder C	274	1.70	/	7.20	65
Thermal grease	PDMS/Al_2O_3/GO	65	10.65	/	25.50	66
	PDMS/Al_2O_3/LM	100	14	/	36	67
	PDMS/CNTs	130	/	/	30.60	68
	PDMS/CNTs	200	/	/	46.90	68
	PDMS/Al_2O_3/ZnO/Ag	85	/	/	28.50	69
	PDMS/AlN/LM	80	/	/	16	70
	Shin-Etsu X-23	100	14	/	40	/
	Thermalright TF-X	37	1.83	/	4.39	/
	Thermalright TF-8	24	3.34	/	5.10	/

	DOWSIL TC-5026	6	1.11	/	3.20	/
Thermal pad	PDMS/graphite	130	22.40	/	94.70	[71]
	PU/Al_2O_3/LM	250	18.28	/	81.16	[72]
	PDMS/graphene	800	27.70	/	43	[73]
	Epoxy/Cu/CNTs	6	2	/	11.50	[74]
	PDMS/InSn	/	/	/	15	[75]
	Epoxy/BN/CNF	18	8.79	/	33.60	[76]
	Epoxy/BN	18	7.51	/	22.80	[76]
	Laird 720	100	117	/	137	/
	Bergquist 5000S35	100	43	/	63	/
LM and its composites	Ga/GaO	33	/	/	2.60	[77]
	O-GaInSn	110	/	/	13.73	[78]
	O-GaInSn/5% Cu	262	4.07	/	14.83	[78]
	O-GaInSn/10% Cu	247	3.37	/	11.88	[78]
	LM/In/LM	158	/	/	3.60	[79]
	GaInSn	92	/	/	2.50	[80]
Polymer	Polythiophene	2.5	12.23	/	12.80+1.30	[81]
	Polyethylene film	2.7	44.70	/	33.66	[82]
This work	LM/AlN-80 μm	197	/	/	2.71	This work
	LM/AlN-80 μm	143	/	/	2.18	
	LM/AlN-80 μm	114	/	/	1.83	
	LM/AlN-30 μm	50	0.12	/	0.86	
	LM/AlN-30 μm	38	0.076	/	0.67	
	LM/AlN-5 μm	22	/	/	0.62	
	LM/AlN-5 μm	13.5	/	/	0.43	
	LM/AlN-1 μm	10.5	/	/	0.42	

Abbreviations: CNTs - carbon nanotubes; P3HT - poly-3-hexylthiophene; PyprPA - pyrenylpropyl phosphonic acid; APS - aminopropyl-trialkoxy-silane; CuNW – copper nanowire; PDMS - polydimethylsiloxane; GO - graphene oxide; CNF – carbon nanofiber; O-GaInSn – oxidized GaInSn

Section 8

Comparison with commercial LM-based thermal pastes

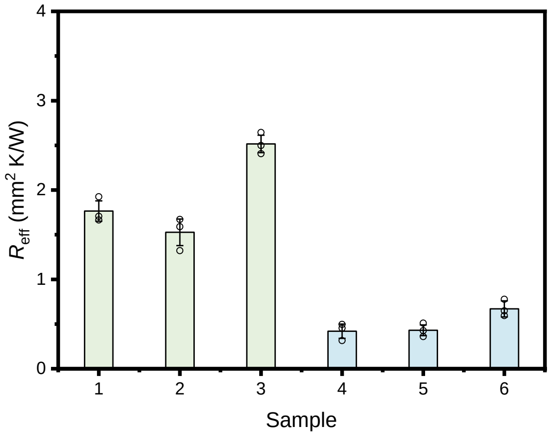

Supplementary Fig. 2 | Comparison with commercial LM-based thermal pastes. *Effective interface thermal resistance of the different LM-based thermal pastes. Sample 1 is CoolLaboratory Liquid Pro, Sample 2 is Thermal Grizzly Conductonaut, Sample 3 is Thermalright Silver King, Sample 4 is LM/1 μm AlN, Sample 5 is LM/5 μm AlN, and Sample 6 is LM/30 μm AlN. The data points and error bars show the mean ± s.d. (sample size 3).*

CoolLaboratory Liquid Pro and Thermal Grizzly Conductonaut are fully liquid-state commercial LM thermal pastes. Thermalright Silver King is an LM alloy paste with *k* claimed as high as 79 W/m K, obtained from Amazon. For these three commercial LM thermal pastes, the interface thermal resistances characterized using the ASTM D5470 method are as follows: 1.77±0.11 mm^2 K/W for CoolLaboratory Liquid Pro, 1.53±0.15 mm^2 K/W for Thermal Grizzly Conductonaut, and 2.52±0.10 mm^2 K/W for Thermalright Silver King (Supplementary Fig. 2). In comparison, the colloidal LMs with varying AlN sizes at their optimal state demonstrated R_{eff} values of 0.42±0.08 mm^2 K/W (LM/1 μm AlN), 0.43±0.06 mm^2 K/W (LM/5 μm AlN), and 0.67±0.09 mm^2 K/W (LM/30 μm AlN), respectively.

Section 9

Large-scale thermal management system and its operations

The large thermal management system (Fig. 4a) comprises three main components: a microchannel cooling module, a housing module, and a heating module. To optimize thermal conduction at the interface between the cooling and heating modules, we apply the colloidal LMs or other TIMs.

The microchannel heatsink is fabricated from an Al/diamond composite material, possessing an intrinsic thermal conductivity of up to 600 W/m K. This ensures highly efficient thermal conduction within the scalable microchannel heatsink, measuring 50 mm×100 mm (Fig. 4b). In order to accommodate the extreme hardness of the embedded diamond particles, a water-assisted laser processing method was employed in its fabrication. The microchannels adopt a deep V-shaped configuration due to the Gaussian distribution of laser energy, with a duty ratio of 1:3. Each parallel microchannel showcases dimensions of 120 μm in width, 600 μm in depth, and an overall thickness of 2 mm (Fig. 4c). Within these microchannels, deionized water acts as the coolant, flowing along the 50-mm direction.

The housing module, securely affixed to the microchannel heatsink, comprises a stainless-steel cover plate, a rubber adjust ring, two rubber seal rings, a quartz glass window, and a stainless-steel shell. Given the large size of this microchannel heatsink, the housing module is equipped with two inlets and two outlets, preventing uneven distribution of coolant during thermal management operations. Additionally, sensor attachment points enable real-time monitoring of coolant parameters and the regulation of heat-extraction processes. The coolant pressure drop and fluid flow are typically determined through inlet and outlet pressure measuring points using a differential pressure transmitter (CYQ-3051DP, 0-600 kPa) and a flow meter (CX-M9-SS-Y, 0.5-5 L/min). Four coolant thermometers (KX-WZP-131, 0-100 ^{o}C) provide fluid temperature rise data, facilitating the calculation of heat extraction efficiency.

The heating module comprises an oxygen-free copper block, a housing shell, and eight cartridge heaters (HW-12-500, 10~500 W). The copper block features a temperature measurement array of K-type thermocouples (DS18B20, 20-200 ^{o}C) drilled into the sidewall, with a horizontal interval of 10 mm and a vertical interval of 6 mm between holes (Fig. 4d). These thermocouples enable the measurement of local wall temperature and effective heat flux during heat-dissipation tests. The housing shell (FR-4 material) is filled with thermostable and thermally insulating fibres. It is highly thermally insulating, effectively reducing heat dissipation into the environment. Eight cartridge heaters, each measuring 12 mm in diameter and 150 mm in length, are fixed to the heating module from the bottom of the copper block (Fig. 4d). Each heater is powered by an adjustable 220 V DC power supply (DQ-6000S), providing independently controllable heating power of up to 500 W. As a result, the copper block effectively concentrates and conducts the generated heat from the cartridge heaters to the upper surface. In this study, the heat flux mentioned in the context is the typical value adjacent to the upper surface of the copper block, which was calibrated according to the temperature gradient of the different thermocouple arrays as shown in Fig. 4d. This upper surface, measuring a substantial area of 20×80 mm^2 (Fig. 4e), is coated with various TIMs to minimize the interface thermal resistance between the heat source of the copper block and the microchannel heatsink.

The above three modules are integrated in a flow loop, with a similar sandwiched pressure (about 40 psi) applied between the heat source and microchannel heat sink. Typically, 20 litres of deionized water are stored in a liquid storage tank, which is equipped with pressure openings to release the air pressure generated by the heated evaporation of the cooling fluid. By adjusting the micro gear pump (CS350, 0.5-5 L/min) and the main valve, different cooling fluid flow rates can be achieved in the flow loop. The micro gear pump also provides the necessary pressure for the cooling fluid, facilitating its smooth passage through the microchannels to complete heat exchange. Prior to the experiment, the cooling working medium is heated to boiling by a thermostat (XU-DC-2030) to prevent interference from gases dissolved in the cooling working medium. An adjustable high-power DC power supply is connected in parallel to the heating tubes to accommodate different heat flow densities during the test. The physical quantities recorded by each sensor are uniformly logged by the data logger (TP700), with a sampling period of one second.

Section 10

Supplementary Table 4 | Experimental results of the scalable thermal management device when employing different TIMs. *The data was collected when the device worked for 30 minutes.*

Conditions (W/cm^2)	Air-50	Grease-50	Grease-100	Grease-150	Grease-200	Colloidal LM-50	Colloidal LM-100	Colloidal LM-150	Colloidal LM-200
Coolant flow (L/min)	2.09	2.09	2.09	2.09	2.10	2.10	2.09	2.10	2.09
Inlet temperature (ºC)	20.79	20.49	20.37	20.29	20.41	20.19	20.12	20.13	20.02
Inlet coolant density (kg/m^3)	998.84	998.84	998.84	998.84	998.84	998.84	998.84	998.84	998.84
Outlet temperature (ºC)	22.01	24.47	27.48	30.89	34.63	25.01	29.76	34.22	39.01
Average coolant temperature (ºC)	21.40	22.48	23.93	25.59	27.52	22.60	24.94	27.18	29.52
Average coolant density (kg/m^3)	997.18	996.95	996.62	996.21	995.70	996.92	996.37	995.80	995.14
Average specific heat capacity ($J\ kg^{-1}\ {}^{o}C^{-1}$)	4182.42	4181.70	4180.80	4179.91	4179.00	4181.62	4180.25	4179.15	4178.23
Power of heat source (W)	820	820	1618	2400	3200	820	1620	2405	3200
Heat extraction (W)	177.53	579.06	1034.24	1541.57	2077.47	704.62	1402.07	2058.55	2760.63
Heat extraction efficiency (%)	21.65	70.62	63.92	64.23	64.92	85.93	86.55	85.59	86.27

Section 11

Simulation of high-throughput heat dissipation

Fluid dynamics and thermal properties were simulated across microchannel models by Fluent (2022R1). The heat source was partially modelled to select its top section adjacent to the thermal interface, while the microchannel heatsink was modelled to full size to ensure simulation accuracy, as shown in Extended Data Fig. 9a. The volume inside the flow channels was designated as the fluid domain, while the remaining part is the solid domain. In order to avoid turbulent flow of fluid during simulation, additional fluid inlet/outlet blocks were defined to ensure stable flow. Constant heat flux was defined at the bottom of the heat source.

Numerical method

In this simulation, the heat transfer and fluid flow models are established based on the following assumptions in the numerical simulation:

(1) The fluid domain is laminar and incompressible.

(2) The thermophysical properties of fluid are temperature-dependent.

(3) The processes of flow and heat transfer are in a steady state.

(4) Radiation heat transfer and gravity are neglected.

Based on these assumptions, the governing equations of numerical simulation can be described as follows:

Continuity equation:

$$\nabla \cdot \boldsymbol{u} = 0$$

Momentum equation:

$$(\boldsymbol{u} \cdot \nabla)\rho_l \boldsymbol{u} = -\nabla P + \mu \nabla^2 \boldsymbol{u}$$

Energy equation:

$$\rho_l c_{p,l}(\boldsymbol{u} \cdot \nabla T) = k_l \nabla^2 T$$

Energy equation of the solid substrate and fin:

$$\nabla \cdot (k_s \nabla T) = 0$$

There are some constraints at the solid-liquid interface. The energy equation of fluid and solid can be solved jointly:

$$T_s = T_l$$

$$k_l \frac{\partial T_l}{\partial n} = k_s \frac{\partial T_s}{\partial n}$$

Non-slip boundary condition:

$$\boldsymbol{u}_{s,\Gamma} = \boldsymbol{u}_{l,\Gamma} = 0$$

Boundary condition

The boundary conditions for the computational domain were established as follows:

(1) The fluid inlet was configured as a mass inlet with a flow rate ranging from 0.02495 kg/s to 0.04159 kg/s, equivalent to a volumetric flow rate of 3 L/min to 5 L/min, with a constant temperature of 293.15 K.
(2) The outlet of the microchannel was defined as a pressure outlet with a set pressure of 0 Pa.
(3) A uniform heat flux ranging from 3×10^6 to 5×10^6 W/m² was applied.
(4) No slippage and continuous temperature were assumed at the solid-liquid interface.
(5) An inlet block measuring 20 mm in length was established upstream of the microchannel to promote fluid development prior to entering the channel, and a similar 20 mm outlet block was positioned downstream to prevent backflow.
(6) Given the symmetry of the solid and fluid domains about the central plane, the model was simplified to half its original size to enhance computational efficiency while symmetric boundary conditions were applied to the central plane of both domains.
(7) Adiabatic conditions were imposed on the remaining solid surfaces.
(8) The top face of the fluid domain was subjected to adiabatic and non-slip boundary conditions.

In this simulation, diamond/Al served as the substrate for the microchannel, copper block served as the heat source, and the thermal interface material between the heat source and the microchannel is colloidal liquid metal. The above three materials were characterized by consistent material properties, shown in Supplementary Table 5. Within the microchannel, deionized water is selected as the working fluid. To enhance the fidelity, the physical attributes of deionized water are temperature-dependent.

Supplementary Table 5 | Material parameters for the simulation. *Definition and properties of the materials in the simulation of high-throughput heat dissipation in the large-scale thermal management system.*

Materials	Density ($kg\ m^{-3}$)	Specific heat capacity ($J\ kg^{-1}\ K^{-1}$)	Thermal conductivity ($W\ m^{-1}\ K^{-1}$)
Copper	8978	384	387.6
Diamond/Al	3215	827	648
Colloidal LM TIM	5215	801	65
Water	998.2	4182	0.6

Calculation

The standard SIMPLE algorithm was used for coupling the pressure velocity. The standard format was applied to solve the pressure equation, and the second-order windward format was used to discretize the momentum and energy equations. The solution was convergent when the normalized residuals for the continuity, momentum, and energy equations fell below 10^{-4}, 10^{-6}, and 10^{-9}, respectively. The operation concluded when the residual fell below the specified value or the maximum iteration step was reached. Simulation results are outlined in Supplementary Table 6.

Supplementary Table 6 | Simulation results of the scalable thermal management device. *The heat flux of heat source and coolant volume flow inside the microchannel are varied.*

Heat flux (W/cm^2)	300	300	300	400	400	400	500	500	500
Coolant flow (L/min)	3	4	5	3	4	5	3	4	5
Inlet temperature (ºC)	20	20	20	20	20	20	20	20	20
Inlet coolant density (kg/m^3)	998.84	998.84	998.84	998.84	998.84	998.84	998.84	998.84	998.84
Outlet temperature (ºC)	40.69	35.58	32.53	47.16	40.52	36.46	53.11	45.08	40
Average coolant density (kg/m^3)	994.89	995.62	996.03	993.89	994.92	995.50	992.88	994.22	995.00
Average specific heat capacity (J kg^{-1} ºC^{-1})	4177.96	4178.89	4179.57	4177.16	4177.99	4178.71	4176.78	4177.37	4178.07
Power of heat source (W)	4800	4800	4800	6400	6400	6400	8000	8000	8000
Heat extraction (W)	4317	4335	4359	5666	5708	5725	6906	6976	6955
Heat extraction efficiency (%)	89.94	90.32	90.81	88.53	89.20	89.46	86.33	87.21	86.94
Average interface temperature (ºC)	78.92	74.85	72.12	96.68	91.44	87.82	112.71	106.83	103.13
Maximum node temperature (ºC)	88.39	83.57	80.45	109.97	102.78	98.63	127.62	120.62	116.35

Section 12

Price of colloidal LMs

The Galinstan used in this study was purchased from Hunan Santech Materials Co., Ltd., China. Its price is $0.7 per gram. AlN is a low-cost ceramic filler. Its price is $0.015-0.079 per gram, which can be referred according to the following website: *https://www.alibaba.com/product-detail/Aln-High-Purity-Aluminum-Nitride-Powder_1601044075939.html?spm=a2700.galleryofferlist.p_offer.d_price.1423e54bOBeh5k&s=p*. For the colloidal LM sample with the 42.5-45.0 vol% content of AlN, the material cost is about $0.5 per gram.

Section 13

UFF force field parameters used in Molecular Dynamics simulation

(i) For the force field parameters of Ga, In and Sn

pair coefficient
Al 0.505000 1.178153
Ga 0.415000 1.104809
In 0.599000 1.176081

(ii) For the force field parameters of AlN

pair coefficient
N 0.072 0.915
Al 0.505000 1.178153

bond coefficient
Al-N 224.0 1.9

angle coefficient
Al-N-Al 188.573070 0.343737 0.374972 0.281246
N-Al-N 100.320469 0.317506 0.313225 0.272502

References

1 Xu, S. *et al.* Electric‐field‐assisted growth of vertical graphene arrays and the application in thermal interface materials. *Advanced Functional Materials* **30**, 2003302 (2020).

2 Cui, Y., Qin, Z., Wu, H., Li, M. & Hu, Y. Flexible thermal interface based on self-assembled boron arsenide for high-performance thermal management. *Nature Communications* **12**, 1284 (2021).

3 Zhao, L. *et al.* Liquid metal nano/micro-channels as thermal interface materials for efficient energy saving. *Journal of Materials Chemistry C* **6**, 10611-10617 (2018).

4 Liang, Z. *et al.* General, vertical, three-dimensional printing of two-dimensional materials with multiscale alignment. *ACS Nano* **13**, 12653-12661 (2019).

5 Lin, Y., Chen, Y.-W. & Yang, J.-T. Optimized thermal management of a battery energy-storage system (BESS) inspired by air-cooling inefficiency factor of data centers. *International Journal of Heat and Mass Transfer* **200**, 123388 (2023).

6 Cai, L. *et al.* Soft Composite Gels with High Toughness and Low Thermal Resistance through Lengthening Polymer Strands and Controlling Filler. *Advanced Functional Materials* **33**, 2207143 (2023).

7 Dai, W. *et al.* Metal-level thermally conductive yet soft graphene thermal interface materials. *ACS Nano* **13**, 11561-11571 (2019).

8 Gao, J. *et al.* Lightweight thermal interface materials based on hierarchically structured graphene paper with superior through-plane thermal conductivity. *Chemical Engineering Journal* **419**, 129609 (2021).

9 Dhanalakota, P., Dileep, H., Malla, L. K., Mahapatra, P. S. & Pattamatta, A. A novel integrated flat thermosyphon heat sink for energy-efficient chip-level thermal management in data centers. *Applied Thermal Engineering*, 121667 (2023).

10 Dai, W. *et al.* Ultralow Interfacial Thermal Resistance of Graphene Thermal Interface Materials with Surface Metal Liquefaction. *Nano-Micro Letters* **15**, 9 (2023).

11 Calame, J. P., Myers, R. E., Binari, S. C., Wood, F. N. & Garven, M. Experimental investigation of microchannel coolers for the high heat flux thermal management of GaN-on-SiC semiconductor devices. *International Journal of Heat and Mass Transfer* **50**, 4767-4779 (2007).

12 Tuckerman, D. B. & Pease, R. F. W. High-performance heat sinking for VLSI. *IEEE Electron Device Letters* **2**, 126-129 (1981).

13 Liu, C. & He, Z. High heat flux thermal management through liquid metal driven with electromagnetic induction pump. *Frontiers in Energy* **16**, 460-470 (2022).

14 Saravanan, V. & Kumaraguruparan, G. Thermal management of microwave electronics in the radar system. *ISSS Journal of Micro and Smart Systems* **8**, 143-153 (2019).

15 Zhang, X.-D. *et al.* Experimental investigation of galinstan based minichannel cooling for high heat flux and large heat power thermal management. *Energy Conversion and Management* **185**, 248-258 (2019).

16 van Erp, R., Soleimanzadeh, R., Nela, L., Kampitsis, G. & Matioli, E. Co-designing electronics with microfluidics for more sustainable cooling. *Nature* **585**, 211-216 (2020).

17 Feng, Z., Hu, Z., Lan, Y., Huang, Z. & Zhang, J. Effects of geometric parameters of circular pin-fins on fluid flow and heat transfer in an interrupted microchannel heat sink. *International Journal of Thermal Sciences* **165**, 106956 (2021).

18 Ansari, D. & Jeong, J. H. A silicon-diamond microchannel heat sink for die-level hotspot thermal management. *Applied Thermal Engineering* **194**, 117131 (2021).

19 Deng, Y., Zhang, M., Jiang, Y. & Liu, J. Two-stage multichannel liquid–metal cooling system for thermal management of high-heat-flux-density chip array. *Energy Conversion and Management* **259**, 115591 (2022).

20 Woodcock, C., Yu, X., Plawsky, J. & Peles, Y. Piranha Pin Fin (PPF) — Advanced flow boiling microstructures with low surface tension dielectric fluids. *International Journal of Heat and Mass Transfer* **90**, 591-604 (2015).

21 Green, C., Fedorov, A. G. & Joshi, Y. K. Fluid-to-fluid spot-to-spreader (F2/S2) hybrid heat sink for integrated chip-level and hot spot-level thermal management. *Journal of Electronic Packaging* **131**, 025002 (2009).

22 Yang, Q. *et al.* Flow Boiling of Ammonia in a Diamond-Made Microchannel Heat Sink for High Heat Flux Hotspots. *Journal of Thermal Science* **29**, 1333-1344 (2020).

23 Hanks, D. F. *et al.* Nanoporous membrane device for ultra high heat flux thermal management. *Microsystems & Nanoengineering* **4**, 1 (2018).

24 Raju V S V, R. & Krishnan, S. Experimental investigation of two-phase pumpless loop with aqueous anionic surfactant as working fluid. *International Journal of Thermal Sciences* **154**, 106400 (2020).

25 Kandlikar, S. G., Widger, T., Kalani, A. & Mejia, V. Enhanced Flow Boiling Over Open Microchannels With Uniform and Tapered Gap Manifolds. *Journal of Heat Transfer* **135**, 061401 (2013).

26 Fazeli, A., Mortazavi, M. & Moghaddam, S. Hierarchical biphilic micro/nanostructures for a new generation phase-change heat sink. *Applied Thermal Engineering* **78**, 380-386 (2015).

27 David, M. P. *et al.* Hydraulic and thermal characteristics of a vapor venting two-phase microchannel heat exchanger. *International Journal of Heat and Mass Transfer* **54**, 5504-5516 (2011).

28 Bian, D. D. W. *Enhanced flow boiling heat transfer in microchannels with structured surfaces at varied mass flow rates*, Massachusetts Institute of Technology, (2015).

29 Wang, H., Wu, J. J., Yang, Q., Zhu, X. & Liao, Q. Heat transfer enhancement of ammonia spray cooling by surface modification. *International Journal of Heat and Mass Transfer* **101**, 60-68 (2016).

30 Wang, J.-X., Li, Y.-Z., Zhong, M.-L. & Zhang, H.-S. Investigation on a gas-atomized spray cooling upon flat and micro-structured surfaces. *International Journal of Thermal Sciences* **161**, 106751 (2021).

31 Pais, M. R., Chow, L. C. & Mahefkey, E. T. Surface Roughness and Its Effects on the Heat Transfer Mechanism in Spray Cooling. *Journal of Heat Transfer* **114**, 211-219 (1992).

32 Muthukrishnan, S. & Srinivasan, V. Enhanced Spray Cooling Using Micropillar Arrays: A Systematic Study. *Journal of Heat Transfer* **142**, 092501 (2020).

33 Bostanci, H. *et al.* High heat flux spray cooling with ammonia: Investigation of enhanced surfaces for CHF. *International Journal of Heat and Mass Transfer* **55**, 3849-3856 (2012).

34 Liu, P., Kandasamy, R., Ho, J. Y., Xie, J. & Wong, T. N. Experimental study on heat transfer enhancement using combined surface roughening and macro-structures in a confined double-nozzle spray cooling system. *Applied Thermal Engineering* **202**, 117850 (2022).

35 Wang, J.-X., Li, Y.-Z., Li, G.-C., Xiong, K. & Ning, X. Investigation of a gravity-immune chip-level spray cooling for thermal protection of laser-based wireless power transmission system. *International Journal of Heat and Mass Transfer* **114**, 715-726 (2017).

36 Luo, X. & Liu, S. A microjet array cooling system for thermal management of high-brightness LEDs. *IEEE Transactions on Advanced Packaging* **30**, 475-484 (2007).

37 Wadsworth, D. C. & Mudawar, I. Enhancement of single-phase heat transfer and critical heat flux from an ultra-high-flux simulated microelectronic heat source to a rectangular impinging jet of dielectric liquid. *Journal of Heat Transfer (Transactions of the ASME (American Society of Mechanical Engineers), Series C);(United States)* **114** (1992).

38 Fabbri, M., Jiang, S. & Dhir, V. K. A comparative study of cooling of high power density electronics using sprays and microjets. *J. Heat Transfer* **127**, 38-48 (2005).

39 Huang, Y. *et al.* Experimental investigation on heat transfer and pressure drop characteristics of confined jet impingement boiling on hybrid-structured surface. *Applied Thermal Engineering* **218**, 119320 (2023).

40 Mira-Hernández, C., Weibel, J. A. & Garimella, S. V. Visualizing near-wall two-phase flow morphology during confined and submerged jet impingement boiling to the point of critical heat flux. *International Journal of Heat and Mass Transfer* **142**, 118407 (2019).

41 Zhao, Z., Peles, Y. & Jensen, M. K. Water jet impingement boiling from structured-porous surfaces. *International Journal of Heat and Mass Transfer* **63**, 445-453 (2013).

42 Browne, E. A., Michna, G. J., Jensen, M. K. & Peles, Y. Experimental investigation of single-phase microjet array heat transfer. *Journal of Heat and Mass Transfer* **132**, 041013 (2010).

43 Sarkar, S., Gupta, R., Roy, T., Ganguly, R. & Megaridis, C. M. Review of jet impingement cooling of electronic devices: Emerging role of surface engineering. *International Journal of Heat and Mass Transfer* **206**, 123888 (2023).

44 Bruggeman, V. D. Berechnung verschiedener physikalischer Konstanten von heterogenen Substanzen. I. Dielektrizitätskonstanten und Leitfähigkeiten der Mischkörper aus isotropen Substanzen. *Annalen der physik* **416**, 636-664 (1935).

45 Nan, C.-W., Birringer, R., Clarke, D. R. & Gleiter, H. Effective thermal conductivity of particulate composites with interfacial thermal resistance. *Journal of Applied Physics* **81**, 6692-6699 (1997).

46 Cheng, Z. *et al.* Experimental observation of high intrinsic thermal conductivity of AlN. *Physical Review Materials* **4**, 044602 (2020).
47 Franco Júnior, A. & Shanafield, D. Thermal conductivity of polycrystalline aluminum nitride (AlN) ceramics. *Ceramica* **50**, 247-253 (2004).
48 Fukushima, K., Takezawa, Y. & Adschiri, T. Evaluation of thermal conductive resistance at organic–inorganic interface and effect of interfaces on thermal conductivity of composite materials. *Japanese Journal of Applied Physics* **52**, 081601 (2013).
49 Zheng, K., Zhu, J., Ma, Y.-M., Tang, D.-W. & Wang, F.-S. Interfacial thermal resistance between high-density polyethylene (HDPE) and sapphire. *Chinese Physics B* **23**, 107307 (2014).
50 Chen, J., Xu, X., Zhou, J. & Li, B. Interfacial thermal resistance: Past, present, and future. *Reviews of Modern Physics* **94**, 025002 (2022).
51 Taphouse, J. H. *et al.* Carbon nanotube thermal interfaces enhanced with sprayed on nanoscale polymer coatings. *Nanotechnology* **24**, 105401 (2013).
52 Taphouse, J. H., Smith, O. N. L., Marder, S. R. & Cola, B. A. A pyrenylpropyl phosphonic acid surface modifier for mitigating the thermal resistance of carbon nanotube contacts. *Advanced Functional Materials* **24**, 465-471 (2014).
53 Cross, R. *et al.* A metallization and bonding approach for high performance carbon nanotube thermal interface materials. *Nanotechnology* **21**, 445705 (2010).
54 Kaur, S., Raravikar, N., Helms, B. A., Prasher, R. & Ogletree, D. F. Enhanced thermal transport at covalently functionalized carbon nanotube array interfaces. *Nature Communications* **5**, 3082 (2014).
55 Gong, W. *et al.* Ultracompliant heterogeneous copper–tin nanowire arrays making a supersolder. *Nano Letters* **18**, 3586-3592 (2018).
56 Jing, L. *et al.* 3D graphene-nanowire “sandwich” thermal interface with ultralow resistance and stiffness. *ACS Nano* **17**, 2602-2610 (2023).
57 Barako, M. T. *et al.* Dense vertically aligned copper nanowire composites as high performance thermal interface materials. *ACS Applied Materials & Interfaces* **9**, 42067-42074 (2017).
58 Wang, M. *et al.* Wafer-scale transfer of vertically aligned carbon nanotube arrays. *Journal of the American Chemical Society* **136**, 18156-18162 (2014).
59 Cola, B. A., Amama, P. B., Xu, X. & Fisher, T. S. Effects of growth temperature on carbon nanotube array thermal interfaces. *Journal of Heat and Mass Transfer* **130**, 114503 (2008).
60 Liu, X., Zhang, Y., Cassell, A. M. & Cruden, B. A. Implications of catalyst control for carbon nanotube based thermal interface materials. *Journal of Applied Physics* **104**, 084310 (2008).
61 Yan, Q. *et al.* Soft and self-adhesive thermal interface materials based on vertically aligned, covalently bonded graphene nanowalls for efficient microelectronic cooling. *Advanced Functional Materials* **31**, 2104062 (2021).
62 Dai, W. *et al.* A paper-like inorganic thermal interface material composed of hierarchically structured graphene/silicon carbide nanorods. *ACS Nano* **13**, 1547-1554 (2019).
63 Tan, X. *et al.* Rational design of high-performance thermal interface materials based on gold-nanocap-modified vertically aligned graphene architecture. *Composites Communications* **24**, 100621 (2021).

64 Liang, Q., Yao, X., Wang, W., Liu, Y. & Wong, C. P. A three-dimensional vertically aligned functionalized multilayer graphene architecture: an approach for graphene-based thermal interfacial materials. *ACS Nano* **5**, 2392-2401 (2011).

65 Chiu, C.-P., Maveety, J. G. & Tran, Q. A. Characterization of solder interfaces using laser flash metrology. *Microelectronics Reliability* **42**, 93-100 (2002).

66 Chen, C., He, Y., Liu, C., Xie, H. & Yu, W. Comprehensive excellent performance for silicone-based thermal interface materials through the synergistic effect between graphene and spherical alumina. *Journal of Materials Science: Materials in Electronics* **31**, 4642-4649 (2020).

67 Xie, Z. *et al.* Joint‐Inspired Liquid and Thermal Conductive Interface for Designing Thermal Interface Materials with High Solid Filling yet Excellent Thixotropy. *Advanced Functional Materials* **33**, 2214071 (2023).

68 Yujun, G., Zhongliang, L., Guangmeng, Z. & Yanxia, L. Effects of multi-walled carbon nanotubes addition on thermal properties of thermal grease. *International Journal of Heat and Mass Transfer* **74**, 358-367 (2014).

69 Zeng, X. *et al.* in *2021 22nd International Conference on Electronic Packaging Technology (ICEPT).* 1-4 (IEEE).

70 Han, L., Huiqiang, L., Zuoye, L. & Sheng, C. AlN/Ga-based liquid metal/PDMS ternary thermal grease for heat dissipation in electronic devices. *Rare Metal Materials and Engineering* **47**, 2668-2674 (2018).

71 Smalc, M., Norley, J., Reynolds III, R. A., Pachuta, R. & Krassowski, D. W. in *International Electronic Packaging Technical Conference and Exhibition.* 253-261.

72 Guo, C. *et al.* A thermally conductive interface material with tremendous and reversible surface adhesion promises durable cross-interface heat conduction. *Materials Horizons* **9**, 1690-1699 (2022).

73 Dai, W. *et al.* Multiscale structural modulation of anisotropic graphene framework for polymer composites achieving highly efficient thermal energy management. *Advanced Science* **8**, 2003734 (2021).

74 Zhang, P., Li, Q. & Xuan, Y. Thermal contact resistance of epoxy composites incorporated with nano-copper particles and the multi-walled carbon nanotubes. *Composites Part A: Applied Science and Manufacturing* **57**, 1-7 (2014).

75 Deng, Y. & Jiang, Y. High-performance, safe, and reliable soft-metal thermal pad for thermal management of electronics. *Applied Thermal Engineering* **199**, 117555 (2021).

76 Raza, M., Westwood, A., Stirling, C. & Ahmad, R. Effect of boron nitride addition on properties of vapour grown carbon nanofiber/rubbery epoxy composites for thermal interface applications. *Composites Science and Technology* **120**, 9-16 (2015).

77 Gao, Y. & Liu, J. Gallium-based thermal interface material with high compliance and wettability. *Applied Physics A* **107**, 701-708 (2012).

78 Li, G., Ji, Y., Wu, M. & Ma, H. in *Heat Transfer Summer Conference.* V001T004A004 (American Society of Mechanical Engineers).

79 Huang, K. *et al.* An anti-leakage liquid metal thermal interface material. *RSC Advances* **10**, 18824-18829 (2020).

80 Ji, Y. *et al.* Excellent thermal performance of gallium-based liquid metal alloy as thermal interface material between aluminum substrates. *Applied Thermal Engineering* **166**, 114649 (2020).

81 Singh, V. *et al.* High thermal conductivity of chain-oriented amorphous polythiophene. *Nature Nanotechnology* **9**, 384-390 (2014).

82 Xu, Y. *et al.* Nanostructured polymer films with metal-like thermal conductivity. *Nature Communications* **10**, 1771 (2019).